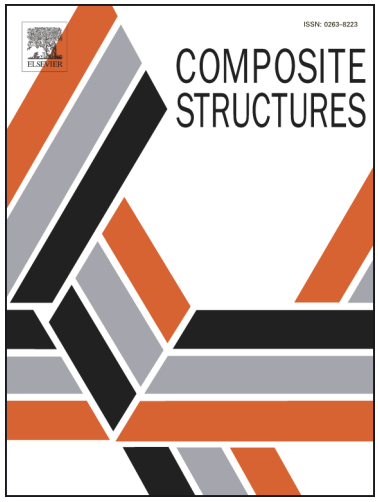

A multi-scale model for studying failure mechanisms of composite blades

Junjie Ye, Chenchen Chu, Heng Cai, Xiaonan Hou, Baoquan Shi, Shaohua Tian, Xuefeng Chen, Jianqiao Ye

PII: S0263-8223(18)33792-9
DOI: https://doi.org/10.1016/j.compstruct.2019.01.031
Reference: COST 10548

To appear in: *Composite Structures*

Received Date: 19 October 2018
Revised Date: 30 December 2018
Accepted Date: 3 January 2019

Please cite this article as: Ye, J., Chu, C., Cai, H., Hou, X., Shi, B., Tian, S., Chen, X., Ye, J., A multi-scale model for studying failure mechanisms of composite blades, *Composite Structures* (2019), doi: https://doi.org/10.1016/j.compstruct.2019.01.031

A multi-scale model for studying failure mechanisms of composite blades

Junjie Ye[1,2], Chenchen Chu[1], Heng Cai[1], Xiaonan Hou[2], Baoquan Shi[1], Shaohua Tian[3], Xuefeng Chen[3], Jianqiao Ye[2,*]

[1]Research Center for Applied Mechanics, Key Laboratory of Ministry of Education for Electronic Equipment Structure Design, Xidian University, Xi'an 710071, China
[2]Department of Engineering, Lancaster University, Lancaster LA1 4YW, UK
[3]State Key Laboratory for Manufacturing Systems Engineering, Xi'an Jiaotong University, Xi'an 710049, China

Abstract

Composite structures have been widely used in wind turbine equipment for their high stiffness to mass ratio and high strength. A major concern in the use of composite materials is their susceptibility to various micro damage, such as fiber breakage and matrix crack, which will lead to macroscopic structural fracture. In this paper, a multi-scale modeling strategy is proposed to investigate failure mechanisms and damage evolution of composite blades with initial defects from microscopic damage (including fiber fractures and matrix cracks) to macroscopic fracture. At the microscopic scale, an isoparametric micromechanical model is developed to calculate microscopic stresses and simulate microscopic damage. At the laminar scale, the classic laminate theory is employed to evaluate the laminate stiffness. At the structural scale, a reverse modeling technology is proposed to accurately acquire structural dimensions of a wind turbine blade, and a macroscopic 3D model is implemented into ANSYS/LS-DYNA software. By comparing with the experimental data, it is demonstrated that the proposed multi-scale method is suitable to predict mechanical properties of complex composite structures effectively.

Keywords: Multiscale model, Wind turbine blade, Composites, Damage evolution, FBG sensors.

1. Introduction

As one of the most abundant renewable and green resources, wind energy is increasingly playing an important role in reducing CO2 emission for environmental protection and has viable commercial values [1-3]. It has been one of the most important new energies due to its availability and accessibility. To maximize the energy that can be harvested from wind, an efficient and safe design of a wind turbine, including its strength and damage tolerance, is essential. Complex dynamic loads may lead to a catastrophic failure of wind turbine blades [4-5]. According to the data from Caithness windfarm information forum [6], blade failure is the most common accident of wind turbines, estimated at around 3800 incidents per annum. Therefore, it is crucial for researchers to have a better understanding of the failure mechanisms, which will improve the safety and reliability of wind turbines.

Wind turbine blades, which are normally manufactured by continuous glass fiber-reinforced resin matrix composites, accounts for nearly one-fifth of the cost of a wind turbine. Experimental [7-8] and theoretical methods [9-10] have been used to investigate the mechanical features and damage mechanisms of composite blades. However, for a heterogeneous material, it is difficult to reveal the intrinsic relations between its macroscopic and microscopic characteristics, such as fiber arrangements and fiber shape [11-14], by experimental methods. As a result, more and more researchers are using numerical methods to study their mechanical properties and optimally design composite wind turbine blades. Haselbach et al. [15] studied ultimate failure of a 34m long blade.

The numerical method the authors used shows good reliability and the obtained results agree well with with the experimental results. Wu et al. [16] developed a GUI interface by using ANSYS to construct a composites blade for stress analysis. The blade skin was designed using the maximum principal stress failure criterion. Rafiee et al. [17] built a 3D finite element model and constructed an iterative fluid-structure interaction approach for investigating aeroelastic behavior of a full-scale composite wind turbine blade. It was concluded that general finite element models for studying composite wind turbine blades were not computationally efficient as a large number of finite elements had to be used. To improve the efficiency, Shah and Tarfaoui [18] proposed a sub-modeling technique to reduce a large finite element model to a more manageable size.

Additionally, failure modes of composites (fiber fracture, matrix crack, etc) are much more complex in comparison with those of homogeneous materials. These failure modes may occur concurrently and at different scales, thereby requiring an integrated multiscale view of the damage evolution starting from initiation, propagation and final structural failure. However, it is difficult for the traditional finite element method to capture all the above events.

Multi-scale methods can be used to capture fine defects and internal cracks in a material and reveal damage evolutions from microscopic damage to macroscopic fracture. Different microstructures and damage modes can be effectively simulated by employing different theories and methods due to the flexibility of multi-scale modeling framework [19-20]. In order to have a better understanding of composite failures, multi-scale methods were proposed to investigate micro/macro-mechanical responses, viscoelastic deformation, failure analysis of composite materials [21-23]. Li and Cui [24] presented a multi-scale analysis method for calculating Yong's modules and Poisson's ratios of composites with random short fiber distributions. Cai and Sun [25] investigated viscoelastic deformations of 3D composites. The results from the multi-scale method agreed well with the experimental results. Moreover, the influence of microscopic structural parameters on viscoelastic properties was studied in details. Calneryte and Barauskas [26] proposed a hierarchical multi-scale approach for studying large displacement, material non-linearity and failure of composites. Zhou et al. [27] proposed a stochastic homogenization method, which coupled with multi-scale homogenization and stochastic finite element methods, to predict effective elastic properties of textile composites. The results showed that the method was sufficiently accurate to acquire elastic properties of the composites. Greco et al. [28] proposed a two-scale finite element continuum approach that was used to compute macroscopic load deflection relationship and predict microscopic local failures. Muliana [29] presented a computational multi-scale model for investigating thermo-viscoelastic responses of spherical particle reinforced polymer matrix composites. Both mechanical and thermal properties of the reinforced particles and polymer matrix were allowed to change with temperature and stress fields. Han et al. [30] employed a hierarchical multi-scale simulation to study thermal residual stresses at microscopic scale and its influences on the strength of composites at macroscopic scale. It revealed that failure modes with and without thermal residual stresses were distinctively different. In regard to applications in turbine blade design, a comprehensive review on damage evolution of wind turbine blades was conducted by Montesano et al. [31], who developed a multi-scale progressive damage model for evaluating sub-critical damage evolution and stiffness degradation of blade structures. The ability of the model to predict the damage was demonstrated by the quasi-static and fatigue simulation results. However, the analyses mentioned above are limited to investigate progressive damages at structural level. For composites, due to their multiphase

structures, it is critical for researchers to reveal multiscale failures of individual constituent materials.

Macroscopic fractures of composite structures are results of microscopic damages. In order to reveal failure mechanisms of composite blades from microscopic damages to macroscopic fractures, a three-scale numerical model is proposed in this study. To verify the proposed method, strain test results acquired by Fiber Bragg Grating (FBG) sensors, which are mounted in the spanwise direction of the composite blades, are employed. Moreover, damage evolutions of reinforced fibers and matrix materials are also investigated. The detailed procedures of the multi-scale modeling, experimental tests and prediction of damage evolutions are explained in the following sections.

2. The multiscale modeling framework

In general, composite blades are composed of thermosetting resin and glass fibers, which are manufactured by manual fiber placement and resin injection technology. The section profile of a composite blade can be considered as a series of laminas with 0° fiber reinforcement [20, 32]. A three-scale method, where macroscopic and microscopic models are coupled first to take advantage of their efficiency and accuracy, respectively, is proposed to investigate the failure mechanisms and damage evolutions of composite blades, as illustrated in Fig. 1. At the microscopic scale, the finite-volume direct averaging micromechanics (FVDAM) theory is used to evaluate the relations between the microscopic structural parameters and the stress-strain properties of the composites. At the laminar scale, the laminate theory is employed to evaluate the stiffness of laminate. A full scale 3D wind turbine blade is stimulated then at the structural scale by ANSYS/LS-DYNA. In order to validate the proposed multi-scale method, the stress-strain curves of a wind turbine blade in the spanwise direction are compared with those from experiments acquired by FBG sensors. The proposed modeling framework is further developed to investigate damage evolutions of the turbine blades by incorporating microscopic damage mechanics, by which the user-defined subroutine of ANSYS/LS-DYNA is utilized to acquire the microscopic stress field. Thus, the damage evolution and constituent failure of wind turbine blades can be further studied. Detailed discussions on damage modeling and failure analysis are finally presented.

3. Multi-scale modeling procedure

3.1. Microscopic modeling of the RVE

In order to analyze microscopic failures of composites, it is important to choose an effective micromechanical method. By employing continuity conditions of sub-cell displacements and stresses, the Generalized Method of Cells (GMC) was proposed by Aboudi [33-34]. The method has been widely used in calculating stiffness matrix, mechanical behavior, as well as microscopic stress fields of composites.

To predict mechanical behaviors of composites accurately, it is critical to define a proper representative volume element (RVE). Compared with overall dimension of a composite structure, the size of the RVE must be sufficiently small. Moreover, the RVE must contain enough information and volume to represent the essence of the microscopic structure. It should be noted that in reality fibers are always randomly distributed in matrix materials [22]. However, in order to simplify the microscopic model, fibers are considered to be periodically distributed in the matrix

materials, and a real composite structure is composed of many of the RVEs. In the procedure of microscopic modeling, a RVE is further divided into sub-cells as shown in Fig. 1(a), where β and γ indicate the serial number of each sub-cell. The dimensions of the RVE in the y_2 and y_3 directions are expressed, respectively, as:

$$H = \sum_{\beta=1}^{N_\beta} h_\beta \quad L = \sum_{\gamma=1}^{N_\gamma} l_\gamma \tag{1}$$

where H and L are dimensions of the RVE as shown in Fig. 1(a). h_β and l_γ are sub-cell dimensions in the y_2 and y_3 directions, respectively.

To improve computational efficiency and accuracy, the GMC was further developed by other researchers [35-36]. By employing the sub-cell stresses as unknown variables, Pindera and Bednarcyk [37] improved calculation efficiency of the microscopic method. In order to further improve the calculation accuracy and solve the sub-cell stress concentrations between inclusions and matrix, an isoparametric element approach was proposed [9, 38]. The relation between the mapping sub-cells in coordinate system $\eta - \xi$ and the sub-cells in coordinate system y_2 - y_3 is given as follows [13]:

$$y_i^{(k)} = N_1(\eta,\xi) y_i^{(1,k)} + N_2(\eta,\xi) y_i^{(2,k)} + N_3(\eta,\xi) y_i^{(3,k)} + N_4(\eta,\xi) y_i^{(4,k)} \quad (i = 2,3) \tag{2}$$

where $N_1(\eta,\xi) = \frac{1}{4}(1-\eta)(1-\xi)$ $N_2(\eta,\xi) = \frac{1}{4}(1+\eta)(1-\xi)$ $N_3(\eta,\xi) = \frac{1}{4}(1+\eta)(1+\xi)$ $N_4(\eta,\xi) = \frac{1}{4}(1-\eta)(1+\xi)$. The superscript, k , denotes serial number of each sub-cell. Superscripts 1-4 are surface numbers of each isoparametric element.

Here, the surface-averaged displacements $\hat{u}_i$ and the surface-average tractions $\hat{t}_i = \sigma_{ij} n_j$ for the kth sub-cell are proposed in the FVDAM theory to substitute the sub-cell displacements in the GMC. σ_{ij} and n_j are stress components and unit normal vectors, respectively. The relationship between the two co-ordinate systems is

$$\begin{bmatrix} \frac{\partial u_i}{\partial \eta} \\ \frac{\partial u_i}{\partial \xi} \end{bmatrix}^{(k)} = \mathbf{J} \begin{bmatrix} \frac{\partial u_i}{\partial y_2} \\ \frac{\partial u_i}{\partial y_3} \end{bmatrix}^{(k)} \tag{3}$$

where $\mathbf{J} = \begin{bmatrix} \frac{\partial y_2}{\partial \eta} & \frac{\partial y_3}{\partial \eta} \\ \frac{\partial y_2}{\partial \xi} & \frac{\partial y_3}{\partial \xi} \end{bmatrix}$ is the Jacobi matrix. For the kth sub-cell, displacement functions $u_i^{(k)}$ can be written in the reference coordinate system (ξ,η) as,

$$\hat{u}_i^{(k)} = W_{i(00)}^{(k)} + \eta W_{i(10)}^{(k)} + \xi W_{i(01)}^{(k)} + \frac{1}{2}(3\eta^2 - 1) W_{i(20)}^{(k)} + \frac{1}{2}(3\xi^2 - 1) W_{i(02)}^{(k)} \tag{4}$$

where $W_{i(00)}^{(k)}$ and $W_{i(mn)}^{(k)} (m \neq 0, n \neq 0)$ are the surface-averaged partial derivatives of the kth

sub-cell displacements.

The relationship between the surface-averaged tractions and the surface-averaged displacements can be expressed as follows:

$$\hat{\mathbf{t}} = \mathbf{NC}\bar{\varepsilon} + \bar{\mathbf{A}}\bar{\mathbf{B}}\hat{\mathbf{u}}' + \bar{\mathbf{A}}\mathbf{N}\boldsymbol{\Phi}^{-1}\mathbf{Z}^{\mathrm{pl}} - \mathbf{N}\boldsymbol{\sigma}^{\mathrm{pl}} \tag{5}$$

where $\hat{\mathbf{t}} = \left[\hat{\mathbf{t}}^{(1)}\ \hat{\mathbf{t}}^{(2)}\ \hat{\mathbf{t}}^{(3)}\ \hat{\mathbf{t}}^{(4)}\ \right]^T$, $\mathbf{N} = \left[\mathbf{n}^{(1)}\ \mathbf{n}^{(2)}\ \mathbf{n}^{(3)}\ \mathbf{n}^{(4)}\ \right]^T$, $\hat{\mathbf{u}} = \left[\hat{\mathbf{u}}^{(1)}\ \hat{\mathbf{u}}^{(2)}\ \hat{\mathbf{u}}^{(3)}\ \hat{\mathbf{u}}^{(4)}\right]$. Detailed expressions of $\bar{\mathbf{A}}$ and $\bar{\mathbf{B}}$ can be found in Khatam [38]. The parameter, $\boldsymbol{\sigma}^{\mathrm{pl}}$, which is determined by matrix plastic deformations, is related to material plastic stress.

To calculate global stiffness matrix $\mathbf{K}_{\mathrm{global}}$ of continuous fiber-reinforced composites, continuity conditions of interfacial traction and displacement across adjacent sub-cells, together with periodic boundary conditions, are imposed. Thus, the following stiffness equation is obtained. The unknown surface-averaged displacements $\mathbf{U}$ is acquired by the global stiffness matrix $\mathbf{K}_{\mathrm{global}}$, that is

$$\mathbf{U} = \mathbf{K}_{\mathrm{global}}^{-1}\left(\Delta\mathbf{C}\bar{\boldsymbol{\varepsilon}} + \boldsymbol{\Gamma}_{\mathrm{global}} + \mathbf{G}_{\mathrm{global}}\right) \tag{6}$$

Where, $\mathbf{U}$ is the unknown surface-averaged displacement; $\bar{\boldsymbol{\varepsilon}}$ is the strain component. $\Delta\mathbf{C}$ contains the sub-cell local stiffness matrix. $\boldsymbol{\Gamma}_{\mathrm{global}}$ and $\mathbf{G}_{\mathrm{global}}$ are related to temperature variations and inelastic properties of the constituent materials.

3.2 Macro modeling of composite laminates

Composite laminates are composed of a serial of laminas. The classic laminate theory calculates the internal in-plane forces $\left[N_{x_1x_1}\ \ N_{x_2x_2}\ \ N_{x_1x_2}\right]^T$ and the internal moments $\left[M_{x_1x_1}\ \ M_{x_2x_2}\ \ M_{x_1x_2}\right]^T$ by the following equations [39]:

$$\begin{bmatrix} N_{x_1x_1} \\ N_{x_2x_2} \\ N_{x_1x_2} \end{bmatrix} = \sum_{k=1}^{N} (C_{ij})^k \int_{x_3(k-1)}^{x_3(k)} \begin{bmatrix} \varepsilon_{x_1x_1} \\ \varepsilon_{x_2x_2} \\ \varepsilon_{x_1x_2} \end{bmatrix} dz \tag{7}$$

$$\begin{bmatrix} M_{x_1x_1} \\ M_{x_2x_2} \\ M_{x_1x_2} \end{bmatrix} = \sum_{k=1}^{N} (C_{ij})^k \int_{x_3(k-1)}^{x_3(k)} z \begin{bmatrix} \varepsilon_{x_1x_1} \\ \varepsilon_{x_2x_2} \\ 2\varepsilon_{x_1x_2} \end{bmatrix} dz \tag{8}$$

where $\left[\varepsilon_{x_1x_1}\ \ \varepsilon_{x_2x_2}\ \ \varepsilon_{x_1x_2}\right]^T$ denote strain components in the $x_1 - x_2$ coordinate system, as shown in Fig. 1(b). $(C_{ij})^{(k)}$ and z are the stiffness matrix and thickness coordinate of the kth lamina, respectively.

The in-plane strain components can be calculated by

$$\begin{bmatrix} \varepsilon_{x_1x_1} \\ \varepsilon_{x_2x_2} \\ 2\varepsilon_{x_1x_2} \end{bmatrix} = \begin{bmatrix} \varepsilon^0_{x_1x_1} \\ \varepsilon^0_{x_2x_2} \\ 2\varepsilon^0_{x_1x_2} \end{bmatrix} + z \begin{bmatrix} k^0_{x_1x_1} \\ k^0_{x_2x_2} \\ 2k^0_{x_1x_2} \end{bmatrix} \tag{9}$$

where $\begin{bmatrix} \varepsilon^0_{x_1x_1} & \varepsilon^0_{x_2x_2} & 2\varepsilon^0_{x_1x_2} \end{bmatrix}^T$ are the mid-surface strains of each lamina. $\begin{bmatrix} k^0_{x_1x_1} & k^0_{x_2x_2} & 2k^0_{x_1x_2} \end{bmatrix}^T$ are the mid-surface curvature and twist.

Substituting Eq. (9) into Eq. (7) and Eq. (8), the equilibrium equation of a composite laminate can be expressed in matrix form as,

$$\begin{bmatrix} N_{x_1x_1} \\ N_{x_2x_2} \\ N_{x_1x_2} \\ M_{x_1x_1} \\ M_{x_2x_2} \\ M_{x_1x_2} \end{bmatrix} = \begin{bmatrix} A_{11} & A_{12} & A_{13} & B_{11} & B_{12} & B_{13} \\ A_{21} & A_{22} & A_{23} & B_{21} & B_{22} & B_{23} \\ A_{31} & A_{32} & A_{33} & B_{31} & B_{32} & B_{33} \\ B_{11} & B_{12} & B_{13} & C_{11} & C_{12} & C_{13} \\ B_{21} & B_{22} & B_{23} & C_{21} & C_{22} & C_{23} \\ B_{31} & B_{32} & B_{33} & C_{31} & C_{32} & C_{33} \end{bmatrix} \begin{bmatrix} \varepsilon_{x_1x_1} \\ \varepsilon_{x_2x_2} \\ 2\varepsilon_{x_1x_2} \\ \varepsilon_{x_1x_1} \\ \varepsilon_{x_2x_2} \\ 2\varepsilon_{x_1x_2} \end{bmatrix} \tag{10}$$

where the elements in equation (10) are calculated by:

$$A_{ij} = \sum_{k=1}^{N} (C_{ij})^k (z_k - z_{k-1}) \quad B_{ij} = \frac{1}{2} \sum_{k=1}^{N} (C_{ij})^k (z_2^2 - z_{k-1}^2) \quad C_{ij} = \frac{1}{3} \sum_{k=1}^{N} (C_{ij})^k (z_2^3 - z_{k-1}^3) \tag{11}$$

3.3 Macroscopic modeling of wind turbine blade

3.3.1 Experimental instrument

In order to study failure mechanisms and damage evolution of composite structures, a wind turbine blade with initial damage is considered, as shown in Fig. 1(c). Due to the complex geometric profile, it is difficult to construct a 3D model using CAD. In order to precisely acquire actual structure parameters of the wind turbine blade, a nonparametric modeling technology based on the reverse engineering is proposed in this study. The experimental equipment includes 3D scanner MetraSCAN and Creaform C-Track as shown in Fig. 2. The laser scanner MetraSCAN can measure an area of 275×250 mm each time with an error tolerance of 0.03mm, and record 480000 points per second. The Creaform C-Track system is used to establish a virtual global coordinate system. Software, Vxinspect and Geomagic Studio, are used to process the data to construct accurate 3D blade models.

3.3.2. Digital modeling of the wind turbine blade

Detailed procedures of the digital modeling of wind turbine blade can be divided into four steps:

(1) Presetting of a measurement system. In order to acquire an accurate 3D model, the wind turbine blade is firstly placed on a platform. The C-Track system, a trilinear coordinate measuring instrument, is fixed to the ground. There must be no obstacle between the camera of the C-Track system and the wind turbine blade.

(2) Acquisition of point clouds. A virtual global coordinate system created by the C-Track

system, is employed to track the wind turbine blade, and connect to the scanner, MetraSCAN. Due to the limited measuring area of 275×250 mm, multi-view point clouds are acquired by the Vxinspect software through moving the MetraSCAN scanner around the wind turbine blade, as shown in Fig. 3.

(3) Data processing of point clouds. Originally scanned point clouds may contain noises or redundancies as shown in Figs. 3(c)-(d). In order to overcome these problems, point clouds are firstly feed into the processing software, Geomagic Studio, to remove noises. Secondly, multi-view point clouds are used to remove redundancies. After the above modifications, a clean, nonoverlapping and smooth point cloud model is obtained.

(4) Surface reconstruction. The processed point cloud model is imported into the Geomagic Studio to reconstruct a fine 3D model. Firstly, the point cloud model is wrapped into a grid model. Secondly, the grid model is further modified by hole filling and remeshing, etc. Finally, on the basis of the mesh model, a smooth surface model is developed by using non-uniform rational B-splines (NURBS) surface fitting technique, as shown in Fig. 4.

To complete the NURBS surface fitting, the cloud data are further reduced according to accuracy requirements. The interpolation function P of the free-form surface can be written as:

$$P(u,v)=\sum_{i=1}^{m+1}\sum_{j=1}^{n+1}p_{ij}N_{i,p}(u)N_{j,q}(v) \tag{12}$$

where p_{ij} donate the control points. $N_{i,p}(u)$ and $N_{j,q}(v)$ are the base functions along the u and v directions, respectively, as shown in Fig. 3(b).

The control points p_{ij}, which are related to weighting factors w_{ij}, can be expressed as [40]

$$p_{ij}(u,v)=\frac{\sum_{i=1}^{m+1}\sum_{j=1}^{n+1}w_{ij}d_{ij}N_{i,p}(u)N_{j,q}(v)}{\sum_{i=1}^{m+1}\sum_{j=1}^{n+1}w_{ij}N_{i,p}(u)N_{j,q}(v)} \tag{13}$$

It should be noted that the free-form surface with a higher accuracy will be generated when the weighting factors w_{ij} are introduced in the interpolation function.

4. Model validation

4.1. Model errors and mesh convergence

4.1.1. Error evaluations of the geometry of the composite blade

The digital geometric profile of the wind turbine blade developed by the MetraSCAN system is shown in Table 1. It can be seen that the measured length and width of the composite blades is 84.5cm and 16.3cm, respectively. For the composite blades, the 3D scanner MetraSCAN can measure an area of 275×250 mm each time with an error tolerance of 0.03mm. It is indicated that the error derived from experimental equipment is acceptable. In order to estimate the accuracy of CAD model reconstruction, the distances between the NURBS surface and point cloud data from the 3D scanner MetraSCAN are compared by employing the Imageware software as shown in Fig. 5. The red surface in Fig. 5(a) shows that the distance errors between the point cloud data and the

NURBS surface can be ignored, and the maximum error, located around the blade tip, is 2.98×10^{-5}mm (as shown in Fig. 5(b)).

4.1.2. Mesh convergence investigations

In this study, 3D FE models with 2212 elements and 65690 elements are used to study mesh sensitivities. The distance between the loading location and the blade tip is 40 mm, and the blade is clamped at the root. The models are subjected to the displacement loadings. Von Mises stresses at four locations, i.e., pt1, pt2, pt3 and pt4, as shown in Fig. 6(a) are compared in Fig. 7. It can be seen that the 3D composite blade model with 2212 elements is sufficiently accurate.

4.2. Comparisons of mechanical properties

4.2.1. Constituent material parameters

The wind turbine blade investigated in this paper is manufactured by E-glass/resin composites. The E-glass fibers are continuously distributed in the matrix. Based on the microscopic images from a transmission electron microscopy test, it is assumed that the fibers are of circular section and periodically distributed in the matrix material. The material parameters of the composite are presented in Table 2, showing that the fibers are transversely isotropic, and the matrix is isotropic.

4.2.2. Load-strain relation

In order to validate the proposed multi-scale model, Fiber Bragg Gratings (FBG) sensors are mounted in the spanwise direction of the blade to acquire real-time strains. Locations of the FBG sensors are labeled as A1-A4 and B1-B4, as shown in Fig. 6(a). It should be noted that a circular hole of $\Phi13$mm located at middle of the chord line and 175mm away from the blade root, presents as an initial defect. To measure stress concentrations, sensors A1 and B1 are located near the initial damage. The strain measurement system is composed of a SM130-700 demodulator, FBG sensors and PC, as shown in Fig. 8. In the experiment, six different loads (1.8kg, 2.8kg, 3.8kg, 4.8kg, 5.1kg and 7.1kg) are applied to the blade tip as shown in Fig. 6(a).

It should be noted that variations of the loadings will lead to strain changes at the measured positions. Accordingly, central wavelengths of the FBG sensors will shift. In order to avoid the wavelength aliasing, FBG sensors with eight different central wavelengths are employed, as shown in Table 3. The relationship between the central wavelengths of the FBG sensors and the measured strains can be written as:

$$\varepsilon = \frac{\Delta\lambda_B}{P_e}\times1000 = \frac{\lambda_B-\lambda_0}{P_e}\times1000 \tag{14}$$

where $\Delta\lambda_B$ is variation of central wavelength. λ_B and λ_0 are current and original wavelength of the FBG sensors, respectively. The conversion coefficient P_e is taken as 1.2 $pm/\mu\varepsilon$ in the experiment.

Figs. 9(a)-(b) present the measured strains relative to the spanwise locations. For comparisons, strain responses of the blade subjected to the six static loads are considered. It is no doubt that the initial damage reduces load carrying capacity of the blade, and stress concentration occurs near the damage. From the tested results, it is interesting to notice that the strain increased first and then decreased in the spanwise direction. The maximum strains are located at A2 and B2, whose locations are 290mm away from the fixed end. This is due to the complex curved surface of the blade aerofoil, as shown in Fig. 6(b).

In order to further verify the method, comparisons between the numerical results and

experimental data are shown in Figs. 10(a)-(b). In general, the predicted strain-load curves agree well with the experimental data. In addition, it appears that the relations between loads and strains are virtually linear, suggesting that plastic deformation of the wind turbine blade is negligible with the range of loading.

5. Damage evolution of the wind turbine blade

5.1. Damage criterion of the constituent materials

In order to study the failure mechanisms and damage evolutions of the composite blade, it is critical to choose a proper failure criterion. Due to the complexities involved in the failures of composites, various criteria have been proposed [41-42]. Tsai-Hill failure criterion, which is considered to be an extension of Von-Mises yield criterion, is suitable to investigate failures of isotropic and anisotropic materials [43]. With consideration of matrix and fiber failures at microscopic scale, the 3D Tsai-Hill criterion is further modified as follows:

$$\begin{aligned}&\left(\left(\sigma_{11}^{(\beta\gamma)}\right)^2+\left(\sigma_{22}^{(\beta\gamma)}\right)^2+\left(\sigma_{33}^{(\beta\gamma)}\right)^2\right)\Big/Y_t^2+\left(-\sigma_{11}^{(\beta\gamma)}\sigma_{22}^{(\beta\gamma)}-\sigma_{11}^{(\beta\gamma)}\sigma_{33}^{(\beta\gamma)}-\sigma_{22}^{(\beta\gamma)}\sigma_{33}^{(\beta\gamma)}\right)\Big/Y_t^2\\&+\left(\left(\sigma_{12}^{(\beta\gamma)}\right)^2+\left(\sigma_{13}^{(\beta\gamma)}\right)^2+\left(\sigma_{23}^{(\beta\gamma)}\right)^2\right)\Big/T^2=D^{(\beta\gamma)}\qquad(\sigma_{22}^{(\beta\gamma)}>0)\end{aligned}\tag{15}$$

where $\sigma_{ij}^{(\beta\gamma)}(i,j=1,2,3)$ are the sub-cell average stresses. $\sigma_{22}^{(\beta\gamma)}>0$ implies that the criterion applied only when the transversal stresses of sub-cells are tensile. Y_t and T are tensile strength and shear strength of matrix materials or fibers. $D^{(\beta\gamma)}$ denotes failure index.

For compressive transverse stresses, the following failure criterion applies:

$$\begin{aligned}&\left(\left(\sigma_{11}^{(\beta\gamma)}\right)^2+\left(\sigma_{22}^{(\beta\gamma)}\right)^2+\left(\sigma_{33}^{(\beta\gamma)}\right)^2\right)\Big/Y_c^2+\left(-\sigma_{11}^{(\beta\gamma)}\sigma_{22}^{(\beta\gamma)}-\sigma_{11}^{(\beta\gamma)}\sigma_{33}^{(\beta\gamma)}-\sigma_{22}^{(\beta\gamma)}\sigma_{33}^{(\beta\gamma)}\right)\Big/Y_c^2\\&+\left(\left(\sigma_{12}^{(\beta\gamma)}\right)^2+\left(\sigma_{13}^{(\beta\gamma)}\right)^2+\left(\sigma_{23}^{(\beta\gamma)}\right)^2\right)\Big/T^2=D^{(\beta\gamma)}\qquad(\sigma_{22}^{(\beta\gamma)}<0)\end{aligned}\tag{16}$$

where Y_c is the compressive strength of matrix materials or fibers. Once the damage index $D^{(\beta\gamma)}$ is equal to 1, fibers or matrix is considered to be failed.

5.2. Multi-scale damage analysis

Fig. 11 illustrates the three-scale damage modeling procedure of the wind turbine blade. The major steps are summarized as follows:

(1) Construct the geometry and define the model based on the data from the Geomagic Studio.

(2) Apply time-dependent loadings and calculate the macroscopic strain components ε_{ij} of each element by finite element (FE) model.

(3) Use the user-defined subroutine of FVDAM in the process of calculations at each integration point of the finite elements at the microscopic scale, as shown in Fig. 11(b). The sub-cell stress/strain fields are solved next by employing the macroscopic strain at each integral point.

(4) Apply failure criteria to identify failures of matrix or fibers. Once one of failure criteria in

Eqs. (15)-(16) is satisfied, the sub-cell stiffness will degenerate to 1% of the original value. In addition, the macroscopic stiffness matrices and the stresses of each finite element are calculated using the homogenization method.

(5) Repeat the above calculations for next loading level and identify newly failed elements. The multi-scale progressive damage analysis terminates once total failure of the blade occurs.

5.3 Matrix damage evolution in wind turbine blade

Fig. 12 shows damage evolution on the upper surface of the blade using the above validated multi-scale model. In general, it can be seen that matrix damage appears first at the blade root and spreads further in the spanwise direction. With the increase of external loadings, damages are found near the hole. In details, when the external load is equal to 11.96kg, a minor matrix damage is found at the blade root as shown in Fig. 12(a). It means that the stresses at the blade root are greater than those around the hole. When the external loading is increased to 17.14kg as shown in Fig. 12(b), a minor matrix damage is found near the hole. When the external load is equal to 23.12kg as shown in Fig. 12(d), the matrix damage are further extended around the hole and the blade root. Furthermore, matrix damage also starts to appear in the leading edge. When the external load is 31.05kg (Fig. 12(e)) or 33.7kg (Fig. 12(f)), it can be seen that new matrix damage are located at the trailing edge near the initial damage.

Fig. 13 shows damage evolutions on the lower surface of the blade subjected to compressive loadings. When the external load increases to 30.69kg as shown in Fig. 13(a), compressive matrix failure occurs at the leading edge of the blade near the root. When the external load is 33.07kg as shown in Fig. 13(b), compressive matrix damage is found at the trailing edge and the tip of the blade. In addition, it is noticed that compressive damage are further accumulated along the blade edge.

5.4 Fiber damage evolution in the wind turbine blade

Fig. 14 shows the fiber damage evolution relative to the external loads. Initial fiber damage at the blade root is found at a load of 20.39kg, as shown in Fig. 14(a). The fiber failures are due to the coupled matrix damages and stress concentrations at the blade root. As the external load increases, further fiber damage accumulate in the spanwise direction, as shown in Fig. 14(b). However, no evident fiber damage is found near the circular hole. From Fig 12 (c)-(f), it can be found that severe matrix damage occurs when the external load is equal to 20.89kg. This severe matrix damage is caused by fiber fracture. The failure of the fibers results in stress concentrations in the matrix materials around the fractured fibers, which accelerates matrix failures.

6. Conclusions

In this study, a generalized multi-scale model was developed to investigate damage evolutions of a composite blade. The proposed multi-scale model included analyses at microscopic, laminar and structural scales. The microscopic model was used to acquire microscopic stress fields of the representative volume element. In order to describe microscopic damage, microscopic failure criteria were introduced and employed. In addition, a reverse technology was employed to acquire actual structure parameters of the wind turbine blade. By comparing with the experimental results, it was concluded that the proposed multi-scale method could be used to effectively predict mechanical properties of complex composite structures.

The validated model was used then to simulate damage evolution of a wind turbine blade with

an initial damage. The numerical results revealed that matrix damage appeared first in the blade root on the upper surface, and developed further in the spanwise direction. With further increasing of the external load, matrix compressive failures were found near the leading edge and the root of the blade's lower surface. In addition, initial fiber damage appeared first near the blade root. The fiber damage also developed further in the spanwise direction.

Future research on failures due to delamination is required. Studies on the coupling effect of microscopic and macroscopic delaminations are also recommended.

Acknowledgments

This work was supported by the National Natural Science Foundation of China (No. 51675397, 51605365). The National Natural Science Foundation of Shaanxi Province (No. 2018JZ5005). China Scholarship Council (No.201706965037). Fundamental Research Funds for the Central Universities (No.JB180414). The 111 Project (No. B14042). The first author is also grateful to the Engineering Department, Lancaster University for the support he has received during the course of his visit.

References

[1] Varna J, Talreja R. Integration of macro- and microdamage mechanics for the performance evaluation of composite materials. Mech Compos Mater 2012; 48(2): 145-160.

[2] Chen N, Wang Q, Yao LZ, Zhu LZ, Tang Y, Wu FB, Chen M, Wang NB. Wind power forecasting error-based dispatch method for wind farm cluster. J Mod Power Syst Clean Energy 2013; 1(1):65-72.

[3] Eder M. A, Bitsche RD, Belloni F. Effects of geometric non-linearity on energy release rates in a realistic wind turbine blade cross section. Compos Struct 2015; 132: 1075-1084.

[4] Pawar MJ, Amar P, Ravindra N. Experimental investigation and numerical simulation of granite powder filled polymer composites forwind turbine blade: a comparative analysis. Polym Compos 2017; 38(7): 1335-1352.

[5] Wang Y, Zhupanska OI. Lightning strike thermal damage model for glass fiber reinforced polymer matrix composites and its application to wind turbine blades. Compos Struct 2015 132: 1182-1191.

[6] Summary of Wind Turbine Accident data to 30 June 2018. http://www.caithnesswindfarms.co.uk/AccidentStatistics.htm

[7] Zeng J, Song BL. Research on experiment and numerical simulation of ultrasonic de-icing for wind turbine blades. Renew Energ 2017; 113: 706-712.

[8] Kim C, Kim K, Kim H, Paek I, Yoo N, Nam Y, Campagnolo F, Bottasso C. Method to estimate bending moments acting on a wind turbine blade specimen using FBG sensors. In J Precis Eng Man 2012; 13(7): 1247-1250.

[9] Jeong J, Park K, Jun S, Song K, Lee DH. Design optimization of a wind turbine blade to reduce the fluctuating unsteady aerodynamic load in turbulent wind. J Mech Sci Technol 2012; 26 (3): 827-838.

[10] Dai JC, Hu YP, Liu DS, Long X. Calculation and characteristics analysis of blade pitch loads forlarge scale wind turbines. Sci China Technol Sci 2010; 53(5): 1356-1363.

[11] Meng Q, Wang Z. Prediction of interfacial strength and failure mechanisms in particle-reinforced metal-matrix composites based on a micromechanical model. Eng Fract Mech 2015; 142: 170-183.

[12] Ye JJ, Qiu YY, Chen XF, Ma J. Initial and final failure strength analysis of composites based

on a micromechanical method. Compos Struct 2015; 125: 328-335.
[13] Ye JJ, Qiu YY, Chen XF, Zhai Z, Huang CL, Zhang XL. Numerical Investigations of Microscopic Characteristic Influences on the Mechanical Properties of Polymer-Matrix Composites. Polym Compos 2017; 38(12): 2734-2742.
[14] Ye JJ, Cai H, Wang YK., Jing Z, Shi BQ, Qiu YY, Chen XF. Effective mechanical properties of piezoelectric–piezomagnetic hybrid smart composites. J Intel Mater Sys Struct 2018; 29(8) 1711-1723.
[15] Haselbach PU, Branner K. Initiation of trailing edge failure in full-scale wind turbine blade test. Eng Fract Mech 2016; 162:136-154.
[16] Wu WH, Young WB. Structural analysis and design of the composite wind turbine blade. Appl Compos Mater 2012; 19(3-4): 247-257.
[17] Rafiee R, Tahani M, Moradi M. Simulation of aeroelastic behavior in a composite wind turbine blade. J Wind Eng Ind Aerod 2016; 151:60-69.
[18] Shah OR, Tarfaoui M. The identification of structurally sensitive zones subject to failure in a wind turbine blade using nodal displacement based finite element sub-modeling. Renew Energ 2016; 87:168-181.
[19] Meng Q, Li B, Li T, Feng XQ. Effects of nanofiber orientations on the fracture toughness of cellulose nanopaper. Eng Fract Mech 2018; 194:350-361.
[20] Zhai Z. Multiscale modeling based on generalized cell of method and its application in composite structural health monitoring. Xi'an Jiaotong University, 2014.
[21] Meng Q, Li B, Li T, Feng XQ. A multiscale crack-bridging model of cellulose nanopaper. J Mech Phys of Solids 2017; 103: 22-39.
[22] Ye JJ, Chu CC, Wang YK, Qiao XJ, Zhai Z, Chen XF. A multi-scale modeling scheme for damage analysis of composite structures based on the High-Fidelity Generalized Method of Cells. Compos Struct. 2018; 206: 42-53.
[23] Kanouté P, Boso DP, Chaboche JL, Schrefler BA. Multiscale Methods for Composites: A Review. Arch Comput Methods Eng. 2009; 16: 31-75.
[24] Li YY, Cui JZ. The multi-scale computational method for the mechanics parameters of the materials with random distribution of multi-scale grains. Compos Sci Technol 2005; 65(9): 1447-1458.
[25] Cai Y, Sun H. Prediction on viscoelastic properties of three-dimensionally braided composites by multi-scale model. J Mater Sci 2013; 48(19): 6499-6508.
[26] Calneryte D, Barauskas R. Multi-scale evaluation of the linear elastic and failure parameters of the unidirectional laminated textiles with application to transverse impact simulation. Compos Struct 2016; 142:325-334.
[27] Zhou XY, Gosling PD, Pearce CJ. Perturbation-based stochastic multi-scale computational homogenization method for woven textile composites. Int J Solids Struct 2016; 80:368-380.
[28] Greco F, Leonetti L, Lonetti P. A two-scale failure analysis of composite materials in presence of fiber/matrix crack initiation and propagation. Compos Struct 2013; 95(95):582-597.
[29] Muliana AH. Multi-scale framework for the thermo-viscoelastic analyses of polymer composites. Mech Res Commun 2007; 35(1):89-95.
[30] Han G, Guan Z, Li Z, et al. Multi-scale modeling and damage analysis of composite with thermal residual stress. Appl Compos Mater 2015; 22(3):289-305.
[31] Montesano J, Hao C, Singh CV. Development of a physics-based multi-scale progressive damage model for assessing the durability of wind turbine blades. Compos Struct 2016; 141:50-62.
[32] Brndsted P, Nijssen RPL. Advances in Wind Turbine Blade Design and materials. Woodhead Pub.; 2013.
[33] Aboudi J, Arnold SM, Bednarcyk BA. Micromechanics of composite materials-a generalized multiscale analysis approach. Elsevier Science Pub. Ltd.; 2013.

[34] Ye JJ, Chen XF, Zhai Z, Li B, Zi YY, He ZJ. Effects of thermal stress and imperfect interfacial bonding on the mechanical behavior of composites subjected to off-axis loading. Mat Sci Eng A 2010; 527: 7530-7537.
[35] Tang Z, Zhang B. Prediction of biaxial failure envelopes for composite laminates based on generalized method of cells. Compos Part B-Eng 2012; 43:914-25.
[36] Ye JJ , Hong Y, Wang YK, Shi BQ, Zhai Z, Chen XF. Thermal cycling influences on compressive deformations of laminate composites. Polym Compos 2018; DOI: 10.1002/pc.
[37] Pindera MJ, Bednarcyk BA. An efficient implementation of the GMC Micromechanics mode for Multi-phased materials with complex microstructures. NASA; 1997.
[38] Khatam H, Pindera M J. Parametric finite-volume micromechanics of periodic materials with elastoplastic phases. Int J Plasticity 2009; 25(7):1386-1411.
[39] Huang ZM, Zhou YX. Strength of fibrous composites. Zhejiang University Press. 2011.
[40] Jung HB, Kim K. A new parameterisation method for NURBS surface interpolation. Int J Adv Manuf Tech, 2000; 16(11): 784-790.
[41] Pandey A, Arockiarajan A. An experimental and theoretical fatigue study on macro fiber composite (MFC) under thermo-mechanical loadings. Eur J Mech-A/Solids 2017; 66: 26-44.
[42] Talreja R. Assessment of the fundamentals of failure theories for composite materials. Compos Sci Technol 2014; 105: 190-201
[43] Rahaeifard M, Ahmadian M T, Firoozbakhsh K. A strain gradient based yield criterion. Int J Eng Sci 2014; 77: 45-54.0

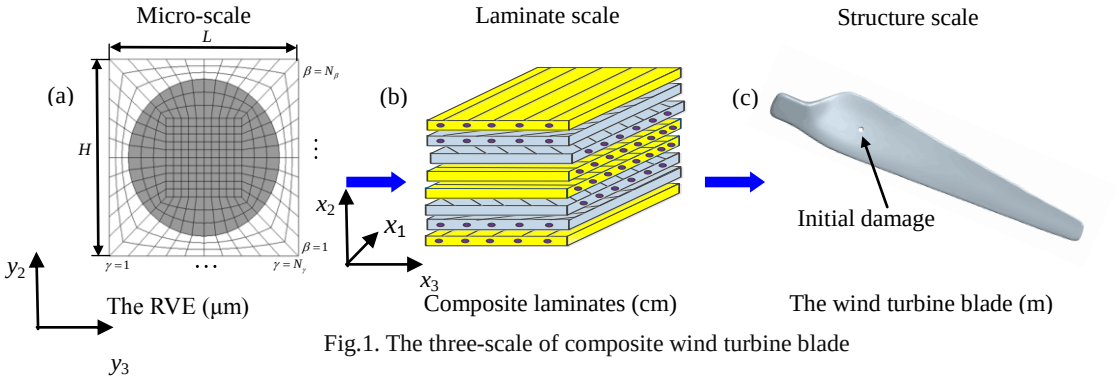

Fig.1. The three-scale of composite wind turbine blade

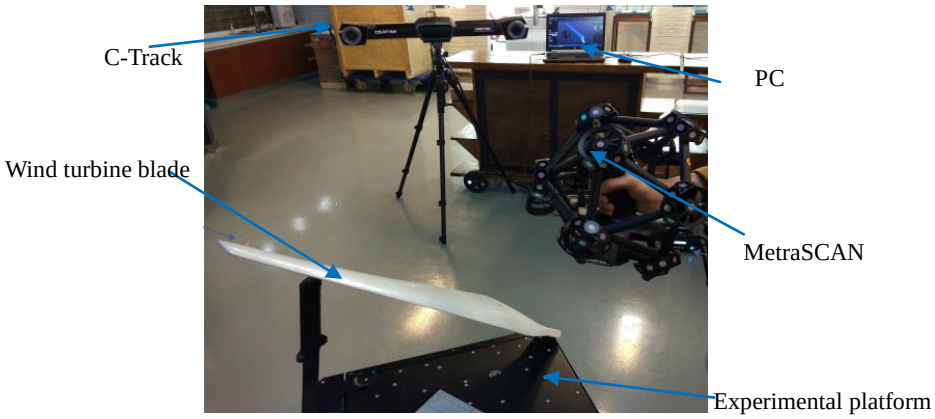

Fig.2. Experimental test system of the 3D blade modeling

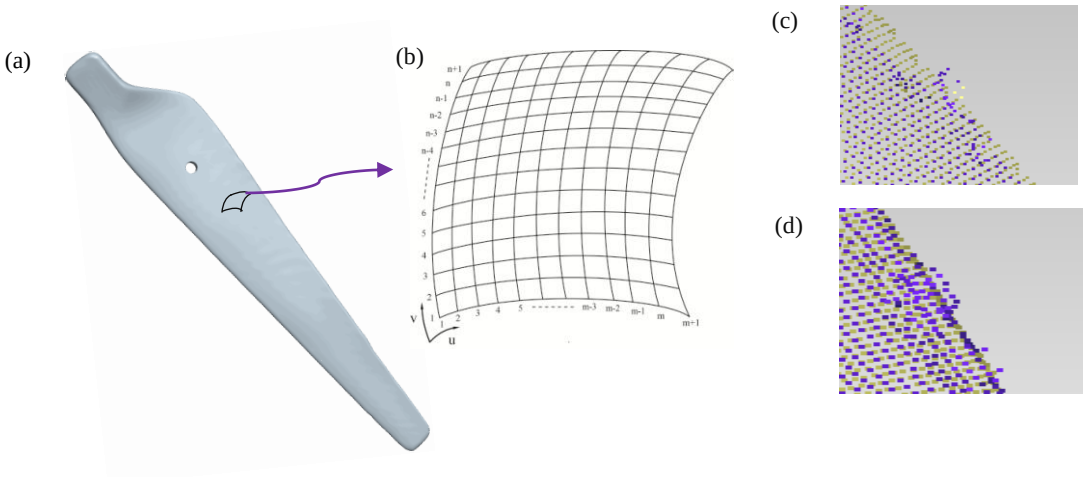

Fig. 3. The originally scanned point cloud data of the wind turbine blade (a) 3D model of a composite blade (b) Partial enlargement surface (c) Redundancies (d) Noises

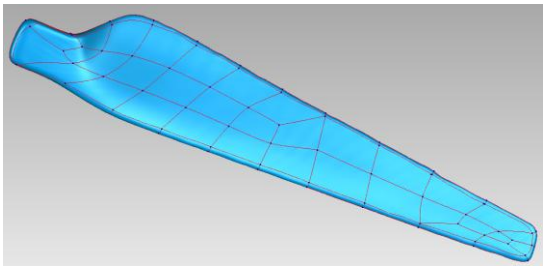

Fig. 4. The NURBS surface model of the wind turbine blade

(a) (b)

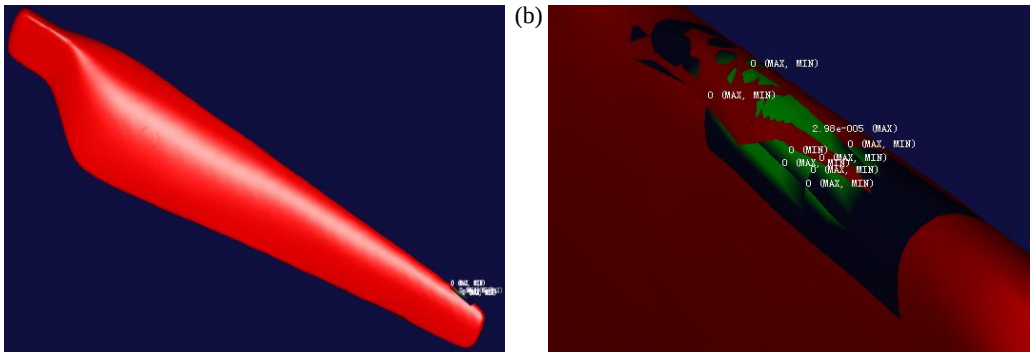

Fig. 5. Error estimations of the 3D model by the Imageware software (a) Distance errors between NURBS surface and point cloud data (b) Partial enlarged graph of the distance errors

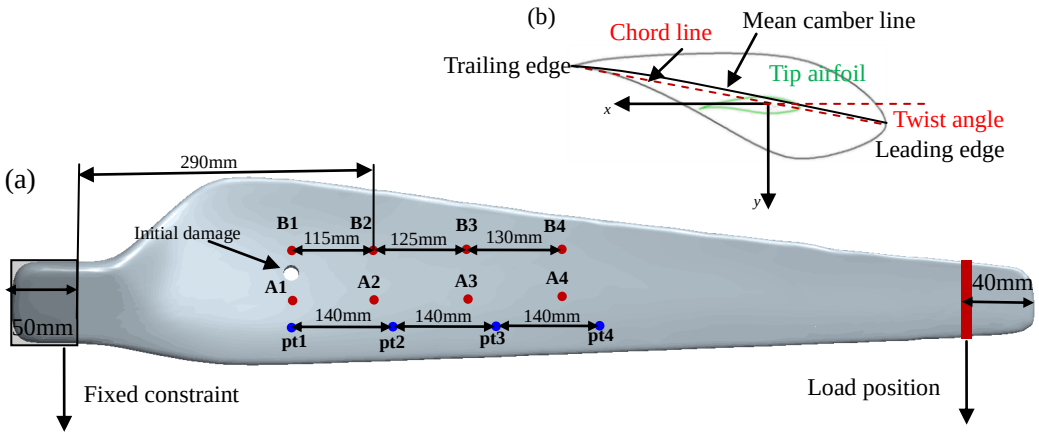

Fig. 6. Layout of the FBG sensors (a) 3D structure of the blade (b) Blade profile

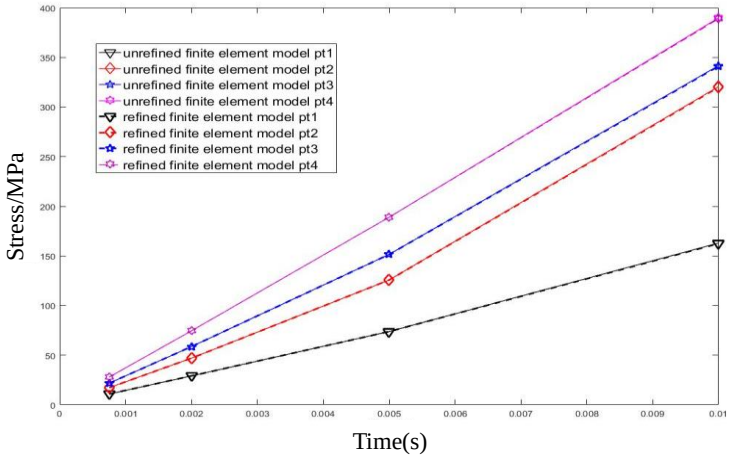

Fig. 7 Mesh convergence investigations

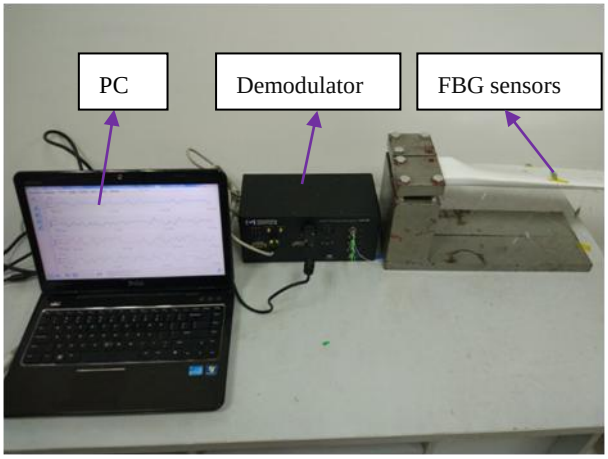

Fig. 8. The experimental system of wind turbine blade

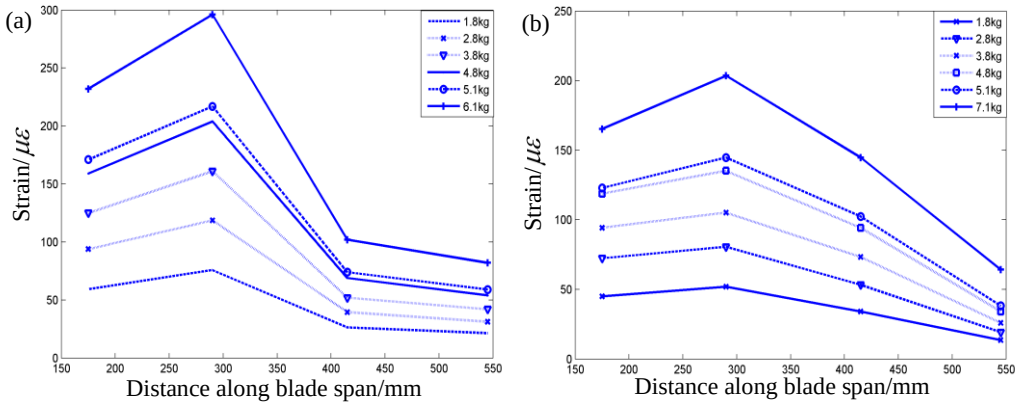

Fig. 9. Strains distribution along the spanwise direction (a) Series A of FBG sensors

(b) Series B of FBG sensors

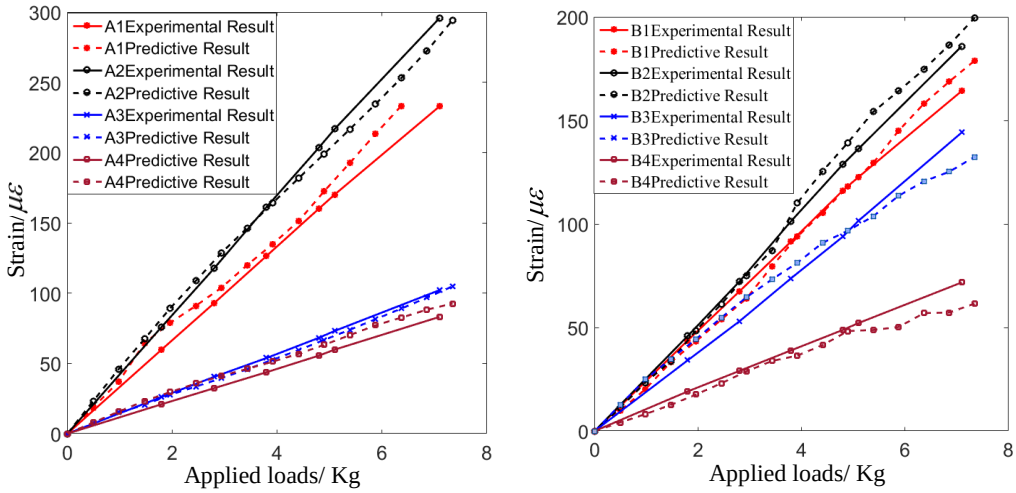

Fig. 10. The comparisons between experimental data and prediction results

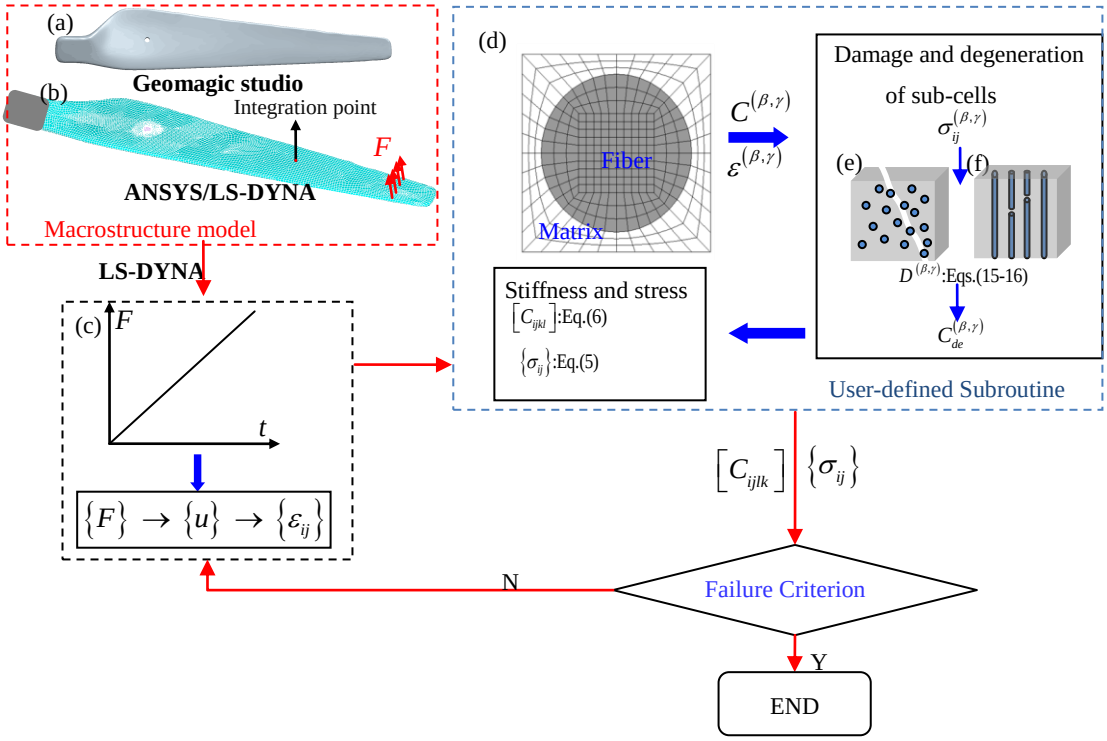

Fig. 11. The implement of modeling and damage analysis for wind turbine blade in three scales (a) 3D digital model of the blade (b) FE model of blade (c) Load increment (d) The RVE (e) Matrix crack (f) Fiber break

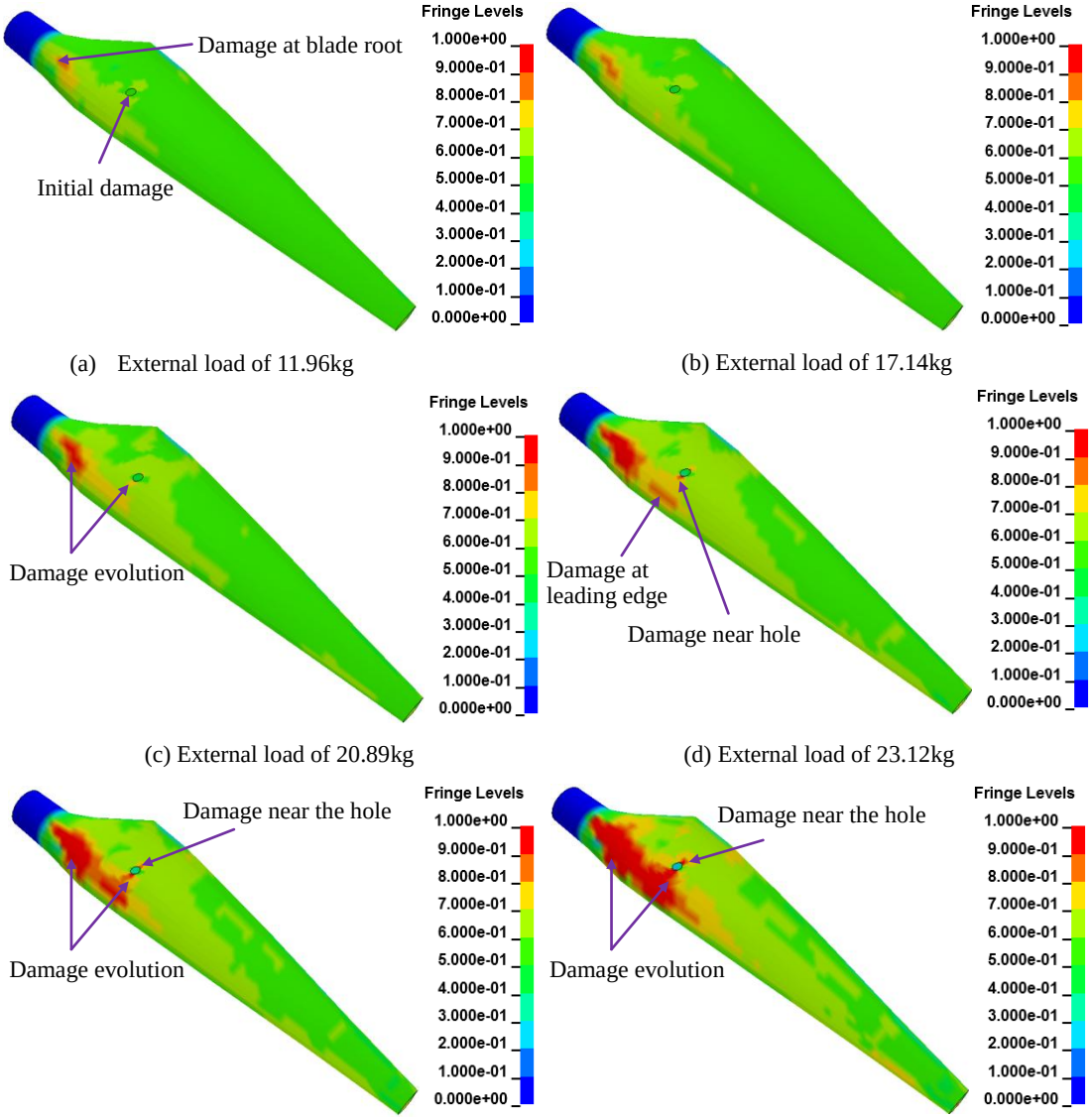

(a) External load of 11.96kg

(b) External load of 17.14kg

(c) External load of 20.89kg

(d) External load of 23.12kg

(e) External load of 31.05kg

(f) External load of 33.7kg

Fig. 12. The matrix damage evolutions of upper surface of wind turbine blade

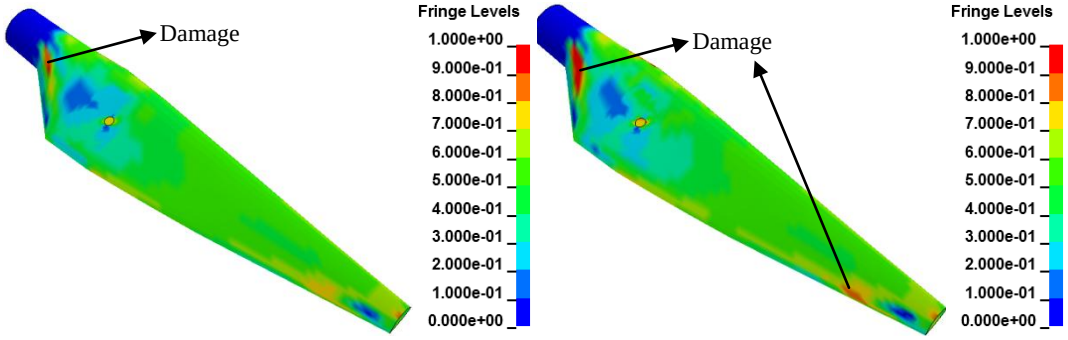

(a)External load of 30.69kg (b) External load of 33.07kg

Fig. 13. The matrix damage evolutions of lower surface of the wind turbine blade

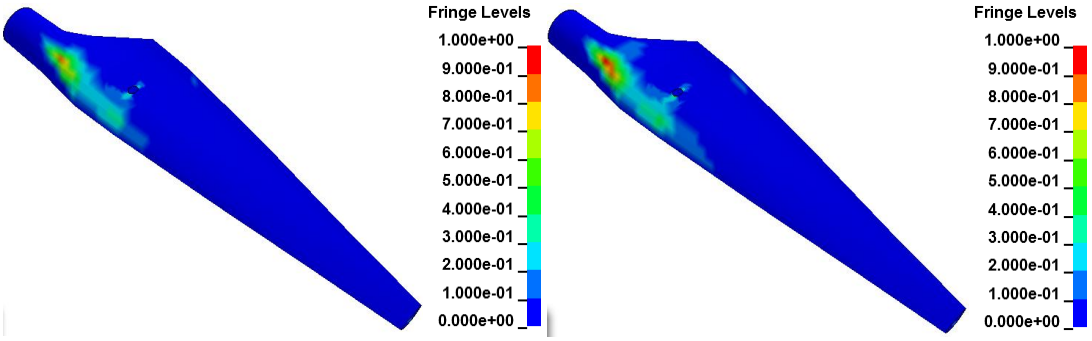

(a) External load of 20.39kg (b) External load of 33.07kg

Fig. 14. The fiber damage evolutions of upper surface of the wind turbine blade

*Corresponding authors.
Email address:j.ye2@lancaster.ac.uk (Jianqiao Ye)

Table 1. Structural parameters of the wind turbine blade

Structural parameters	Length	Maximum chord length	Tip chord length	Root chord length	Initial damage
Value (mm)	845	163	60	68	Φ13

Table 2. Parameters of constituent materials

Materials	E / (GPa)	υ	Y_t / (MPa)	Y_c / (MPa)	T / (MPa)
E-glass	72	0.2	1617	421	37
Resin	3.3	0.22	121	176	50

Table 3 Central wavelength of each FGB sensor

Series of grating	A1	A2	A3	A4	B1	B2	B3	B4
Central wavelengths/nm	1541	1547	1532	1538	1556	1535	1538	1552